Interplay of edge fracture and shear banding in complex fluids

Ewan J. Hemingway, and Suzanne M. Fielding

Citation: Journal of Rheology **64**, 1147 (2020); doi: 10.1122/8.0000086
View online: https://doi.org/10.1122/8.0000086
View Table of Contents: https://sor.scitation.org/toc/jor/64/5
Published by the The Society of Rheology

Interplay of edge fracture and shear banding in complex fluids

Ewan J. Hemingway and Suzanne M. Fielding[a)]

Department of Physics, Durham University, Science Laboratories, South Road, Durham DH1 3LE, United Kingdom

(Received 20 May 2020; final revision received 4 August 2020; published 28 August 2020)

Abstract

We explore theoretically the interplay between shear banding and edge fracture in complex fluids by performing a detailed simulation study within two constitutive models: the Johnson–Segalman model and the Giesekus model. We consider separately parameter regimes in which the underlying constitutive curve is monotonic and nonmonotonic, such that the bulk flow (in the absence of any edge effects) is, respectively, homogeneous and shear banded. Phase diagrams of the levels of edge disturbance and of bulk (or quasibulk) shear banding are mapped as a function of the surface tension of the fluid–air interface, the wetting angle where this interface meets the walls of the flow cell, and the imposed shear rate. In particular, we explore in more detail the basic result recently announced by Hemingway and Fielding [Phys. Rev. Lett. **120**, 138002 (2018)]: that precursors to edge fracture can induce quasibulk shear banding. We also appraise analytical predictions that shear banding can induce edge fracture [S. Skorski and P. D. Olmsted, J. Rheol., **55**, 1219 (2011)]. Although a study of remarkable early insight, Skorski and Olmsted [J. Rheol., **55**, 1219 (2011)] made some strong assumptions about the nature of the "base state," which we examine using direct numerical simulation. The basic prediction that shear banding can cause edge fracture remains valid but with qualitatively modified phase boundaries. © *2020 The Society of Rheology.* https://doi.org/10.1122/8.0000086

I. INTRODUCTION

In many complex fluids, a state of initially homogeneous bulk shear flow is unstable to the formation of coexisting bands of differing shear rate, with layer normals in the flow-gradient direction. This phenomenon, which is called shear banding [3–6], has been observed in wormlike micellar surfactants [7], lyotropic lamellar phases [8], triblock copolymers [9], telechelic polymers [10], star polymers [11], clays [12,13], emulsions [13] and (subject to controversy [14,15]) monodisperse linear entangled polymers [16,17]. It is thought to stem from a nonmonotonicity in the underlying bulk constitutive relation between shear stress and shear rate for homogeneous shear, $\sigma(\dot{\gamma})$. A state of initially homogeneous shear is linearly unstable to the formation of shear bands in the regime of the negative slope, $d\sigma/d\dot{\gamma} < 0$ [18]. The steady state flow curve of shear stress as a function of gap-averaged shear rate, $\sigma(\bar{\dot{\gamma}})$, then displays a plateau over the range of shear rates for which the flow is banded.

Many flow instabilities depend not only on bulk rheology but also on the boundary conditions where the fluid meets the walls of the flow cell and/or the outside air. In the cone–plate device sketched in Fig. 1 (top left), for example, the fluid (shown in blue) has an interface with the air (white). When a highly viscoelastic fluid is strongly sheared, this free surface can destabilize to give a more complicated edge profile, with an indentation that invades the fluid bulk. Some portion of the sample can even be ejected from the device. This phenomenon, which is called "edge-fracture," renders accurate rheological measurements very difficult. Anecdotal reports of edge fracture pervade the experimental literature. Detailed studies can be found in Refs. [19–25].

Pioneering theoretical work by Tanner *et al.* [26,27] identified the second normal stress difference in the sheared fluid, $N_2(\dot{\gamma})$, as a key factor in driving edge fracture, and proposed the criterion for the onset of edge fracture to be $|N_2| > 2\Gamma/3R$, where Γ is the surface tension of the fluid–air interface, and R is the radius of a preassumed indentation in the interfacial profile. Recently, Hemingway *et al.* [28,29] derived an updated criterion,

$$\frac{\sigma}{2}\frac{d|N_2(\dot{\gamma})|}{d\dot{\gamma}} \Bigg/ \frac{d\sigma}{d\dot{\gamma}} > \frac{2\pi\Gamma}{L_y}, \tag{1}$$

and showed it to be in full agreement with numerical simulations. (Here, L_y is the size of the gap between the rheometer plates.) This criterion marks the transition with increasing flow rate (which determines the LHS of the above inequality) or decreasing surface tension (on the RHS) from a state in which the fluid–air interface is undisturbed by flow to one in which it can become significantly deformed, but remains intact overall: i.e., a partially edge fractured state. Full edge fracture, explored by direct numerical simulation [28,29], follows for even stronger flows or smaller surface tensions, with the fluid then completely dewetting the walls.

So far, we have discussed shear banding as a purely bulk instability and edge fracture as an interfacial instability, implicitly suggesting that the two instabilities act independently of each other, and without any interplay between them. Recent work [1], however, showed that even only modest deformations of the fluid–air interface can lead to strong secondary flows in the fluid. For a material with a relatively flat bulk constitutive curve $\sigma(\dot{\gamma})$, these can take the

[a)]Author to whom correspondence should be addressed; electronic mail: suzanne.fielding@durham.ac.uk

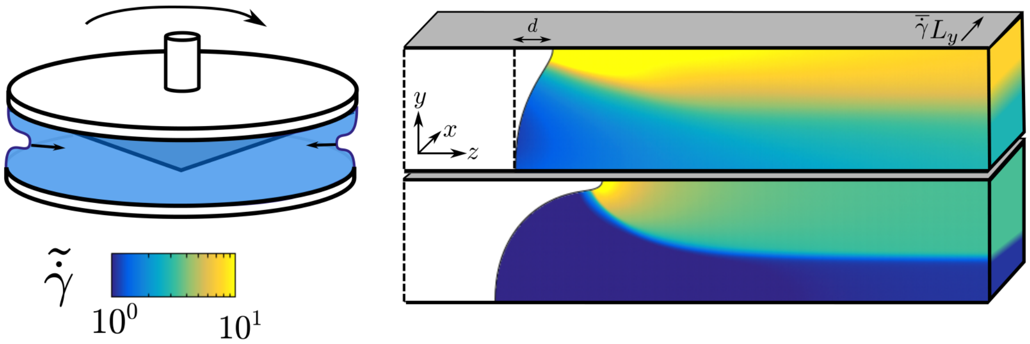

FIG. 1. Top left: schematic of a cone–plate device. Top right: the snapshot of a state in which an edge disturbance induces apparent shear banding that invades far into the bulk. (Giesekus model with a monotonic constitutive curve, $\bar{\dot\gamma} = 4.7$, $\eta_s = 0.006$, $\Gamma = 0.24$.) Bottom right: the snapshot of a state in which shear banding induces a significant edge disturbance. (The Johnson–Segalman model with a nonmonotonic constitutive curve, $\bar{\dot\gamma} = 2.5$, $\eta_s = 0.1$, $\Gamma = 0.11$.) Bottom left: the color scale of invariant shear rate in snapshots.

form of apparent shear bands that invade deep into the bulk, even for a curve that is monotone increasing, $d\sigma/d\dot\gamma > 0$. In this way, precursors of the *interfacial* instability of edge fracture can precipitate quasibulk shear banding. A simulation snapshot of this phenomenon is shown in Fig. 1 (top right). To paraphrase this scenario: "(precursors to) edge fracture can induce (apparent) shear banding." Conversely, in many fluids that show true bulk shear banding (even in the absence of any edge effects), the fluid–air interface often destabilizes above a critical shear rate on the stress plateau of the flow curve, leading to the sample being ejected from the flow device [30,31]. This phenomenon was studied theoretically by Skorski and Olmsted [2], who showed that the fluid–air interface of a shear banded sample must always be at least partially disturbed, with meniscus curvatures set by the jump in second normal stress across the interface between the bulk bands. A simulation snapshot of this phenomenon is shown in Fig. 1 (bottom right). As the relative fraction of the rheometer gap taken up by each band changes with the overall imposed shear rate, one of the bands can develop a width that cannot support the meniscus curvatures demanded by this second normal stress balance, leading to full edge fracture. To paraphrase this scenario, "shear banding can induce edge fracture."

For many years, an outstanding question has been whether the underlying constitutive curve of monodisperse linear entangled polymers is monotonic or nonmonotonic, and so whether a steady applied shear flow should be homogeneous or shear banded. Because the underlying constitutive curve cannot be accessed experimentally in a shear banding system, this question must be settled by explicit velocimetry of the flow field. Tapadia and Wang [32] gave evidence for steady state banding, suggesting a nonmonotonic constitutive curve. In contrast, Hu *et al.* [33] found banding only transiently during shear startup, with homogeneous shear recovered at longer times, suggesting a monotonic constitutive curve. Work on more highly entangled samples did, however, report long-lived bands in some runs, but not others [34], even when repeated for the same imposed flow rates. Edge fracture was discussed as a possible source of this variability. Significant possible edge fracture in experiments investigating shear banding in entangled polymers was likewise discussed in Refs. [35–37].

We have seen, then, that "(precursors to) edge fracture can induce (apparent) shear banding,"that "shear banding can induce edge fracture," and that the relative roles of shear banding and edge fracture remain unclear in some experiments, particularly on linear entangled polymers. Theoretical work is clearly needed, therefore, to disentangle the relative contributions of shear banding and edge fracture in highly viscoelastic fluids and to assess any interplay between them.

The aim of the present manuscript is to explore theoretically this interplay between shear banding and edge fracture, by performing a detailed simulation study within two constitutive models: the Johnson–Segalman model [38] and the Giesekus model [39]. Considering separately parameter regimes in which the underlying constitutive curve is monotonic and nonmonotonic, we shall map out phase diagrams of the levels of edge disturbance and of bulk (or quasibulk) banding as a function of the surface tension of the fluid–air interface, the wetting angle where this interface meets the walls of the flow cell, and the imposed shear rate. In particular, we shall explore in more detail the basic result recently announced in Ref. [1]: that "(precursors to) edge fracture can induce (apparent) shear banding." We also carefully appraise the analytical predictions that "shear banding can cause edge fracture": although a study of remarkable early insight, Ref. [2] made some strong assumptions about the nature of the "base state," which we will now examine using direct numerical simulation.

The paper is structured as follows. In Sec. II, we discuss the theoretical models to be used throughout the paper. In Sec. III, we introduce the flow geometry that we simulate, along with the boundary conditions, initial conditions, and choice of parameter values. We then present our results, starting in Sec. IV with the case of (apparent) shear banding induced by disturbances at the fluid–air interface, for a fluid with a monotonic though relatively flat constitutive curve. We then discuss the case of edge fracture induced by bulk banding, given a nonmonotonic constitutive curve, in Sec. V. Finally, Sec. VI gives our conclusions and perspectives for future work.

II. MODELS

We work in the zero Reynolds number limit of inertialess flow, in which the total stress in any element of fluid or air,

$\mathbf{T}(\mathbf{r}, t)$ (with $\mathbf{r}$ position and t time), must obey the condition of force balance,

$$\nabla.\mathbf{T} = 0. \tag{2}$$

In any element inside the fluid, $\mathbf{T}$ comprises the sum of an isotropic contribution characterized by a pressure $p(\mathbf{r}, t)$, a Newtonian contribution with a viscosity η_s, and a viscoelastic contribution $\mathbf{\Sigma}(\mathbf{r}, t)$ arising from the polymer chains, wormlike micelles, etc. The condition of force balance then reads

$$\eta_s \nabla^2 \mathbf{v} + \nabla.\mathbf{\Sigma} - \nabla p = 0, \tag{3}$$

in which $\mathbf{v}(\mathbf{r}, t)$ is the fluid velocity.

The condition of force balance in the air demands

$$\eta_a \nabla^2 \mathbf{v} - \nabla p = 0. \tag{4}$$

We assume the flow to be incompressible, such that the velocity field $\mathbf{v}(\mathbf{r}, t)$ obeys

$$\nabla.\mathbf{v} = 0. \tag{5}$$

Enforcing this condition determines the pressure, $p(\mathbf{r}, t)$.

We consider two different constitutive models for the dynamics of the viscoelastic stress. The first is the Johnson–Segalman model [38], in which

$$\begin{aligned}\partial_t \mathbf{\Sigma} + \mathbf{v}.\nabla\mathbf{\Sigma} = {} & (\mathbf{\Sigma}\cdot\mathbf{\Omega} - \mathbf{\Omega}\cdot\mathbf{\Sigma}) + a(\mathbf{D}\cdot\mathbf{\Sigma} + \mathbf{\Sigma}\cdot\mathbf{D}) \\ & + 2G(\phi)\mathbf{D} - \frac{1}{\tau(\phi)}\mathbf{\Sigma} + \frac{\ell^2}{\tau(\phi)}\nabla^2\mathbf{\Sigma}.\end{aligned} \tag{6}$$

Here, $\mathbf{D} = \frac{1}{2}(\nabla\mathbf{v} + \nabla\mathbf{v}^T)$ and $\mathbf{\Omega} = \frac{1}{2}(\nabla\mathbf{v} - \nabla\mathbf{v}^T)$ are, respectively, the symmetric and antisymmetric parts of the strain rate tensor, $\nabla\mathbf{v}_{\alpha\beta} = \partial_\alpha v_\beta$. The parameter a, which lies in the range $-1 \le a \le 1$, describes a slippage of the viscoelastic component relative to the solvent. In stationary homogeneous simple shear flow, the constitutive curve $T_{xy}(\dot\gamma) = \Sigma_{xy}(\dot\gamma) + \eta_s\dot\gamma$ is a nonmonotonic function of the imposed shear rate for $|a| < 1$ and $\eta_s < 1/8$. In this regime, a state of steady shear flow is shear banded. For $\eta_s > 1/8$, in contrast, a steady state shear flow must be homogeneous, at least in the absence of any edge disturbances. The second normal stress, $N_2(\dot\gamma) = \Sigma_{yy} - \Sigma_{xx}$, is negative, and scales as $-\dot\gamma^2$ in the limit $\dot\gamma \to 0$.

The second constitutive model that we shall study is the Giesekus model [39], in which

$$\begin{aligned}\partial_t \mathbf{\Sigma} + \mathbf{v}.\nabla\mathbf{\Sigma} = {} & (\mathbf{\Sigma}\cdot\mathbf{\Omega} - \mathbf{\Omega}\cdot\mathbf{\Sigma}) + (\mathbf{D}\cdot\mathbf{\Sigma} + \mathbf{\Sigma}\cdot\mathbf{D}) \\ & + 2G(\phi)\mathbf{D} - \frac{1}{\tau(\phi)}\mathbf{\Sigma} - \frac{\alpha}{\tau(\phi)}\mathbf{\Sigma}\cdot\mathbf{\Sigma} \\ & + \frac{\ell^2}{\tau(\phi)}\nabla^2\mathbf{\Sigma}.\end{aligned} \tag{7}$$

The parameter α in this equation captures an increase in the rate of stress relaxation when the polymer chains are more strongly aligned. In a stationary homogeneous shear flow, the viscoelastic shear stress $\Sigma_{xy}(\dot\gamma)$ is a nonmonotonic function of $\dot\gamma$ for $\alpha > 1/2$, and monotonic for $\alpha < 1/2$ [39]. The second normal stress scales as $-\dot\gamma^2$ at low shear rates, as in the Johnson–Segalman model.

The spatial gradient terms prefactored by ℓ in Eqs. (6) and (7) ensure that the interface between any shear bands has a slightly diffuse thickness that scales as ℓ [40].

We model the coexistence of fluid and air using a phase field $\phi(\mathbf{r}, t)$, which obeys Cahn–Hilliard dynamics [41]

$$\partial_t \phi + \mathbf{v}.\nabla\phi = M\nabla^2\mu. \tag{8}$$

Here, M is a constant molecular mobility. The chemical potential

$$\mu = G_\mu\left(-\phi + \phi^3 - \ell_\mu^2\nabla^2\phi\right), \tag{9}$$

in which the constant parameter G_μ determines the free energy of demixing per unit volume. This captures the coexistence of a fluid phase, in which $\phi = 1$, with an air phase, in which $\phi = -1$. The elastic modulus G and the relaxation time τ in the constitutive Eqs. (6) and (7) are functions of ϕ, with $G(\phi = 1) = 1$, $\tau(\phi = 1) = 1$, and $G(\phi = -1) = 0$, with $\tau(\phi = -1) = 0.002$, such that viscoelastic stresses arise only in the fluid.

The fluid–air interface has a slightly diffuse thickness that scales as the parameter ℓ_μ. This is needed to capture the motion of the contact line where the fluid–air interface meets the walls of the flow cell [42]. Gradients in μ across the interface contribute an additional source term $-\phi\nabla\mu$ to the force balance condition, capturing the effects of the interfacial surface tension. The surface tension is

$$\Gamma = \frac{2\sqrt{2}}{3}G_\mu\ell_\mu. \tag{10}$$

III. FLOW GEOMETRY, BOUNDARY CONDITIONS, AND INITIAL CONDITIONS

We ignore any complications of slight streamline curvature and stress heterogeneity that are present in many common experimental shear cells (cone–plate, plate–plate, cylindrical Couette, etc.), simulating instead a planar slab of fluid between flat parallel plates. The fluid is sheared at an overall imposed rate $\bar{\dot\gamma}$ by moving the top plate at speed $\dot\gamma L_y$ along $\hat{\mathbf{x}}$. See Fig. 2, in which the flow-gradient direction, $\hat{\mathbf{y}}$, and vorticity direction $\hat{\mathbf{z}}$, are, respectively, vertical and horizontal, with the flow direction, $\hat{\mathbf{x}}$, into the page. We assume translational invariance along $\hat{\mathbf{x}}$, setting ∂_x of all quantities equal to zero, performing two-dimensional (2D) simulations in the $y - z$ plane sketched, with all snapshots below also shown in this plane. The velocity vector and stress tensor are nonetheless fully 3D objects.

The simulation box has length L_z in the vorticity direction, with periodic boundary conditions in that direction. At the walls of the flow cell in the gradient direction y, we assume conditions of no slip and no permeation for the fluid velocity

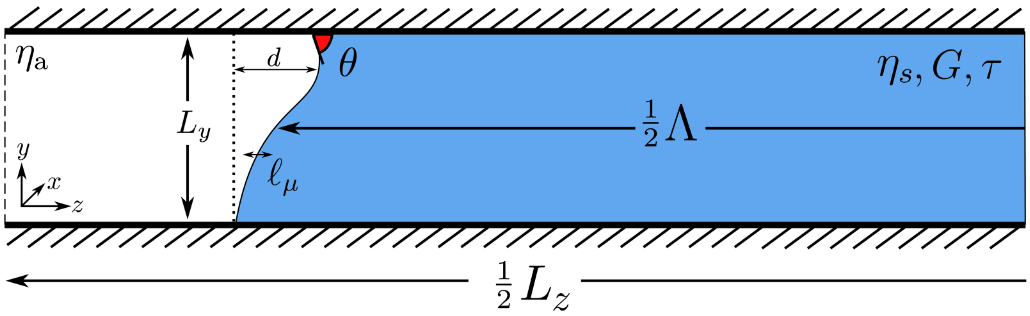

FIG. 2. Flow geometry to be simulated: a planar slab of fluid sandwiched between hard flat parallel plates at $y = \pm L_y/2$. The flow is effected by moving the top plate into the page at speed $\dot{\gamma}L_y$, with the bottom plate stationary. Accordingly, the base state flow (before any secondary flows arise due to the instability of interest here) is of the general form $\mathbf{v} = (v_x(y, z), 0, 0)$. The fluid (shown in blue) meets the air (white) at the fluid–air interface. Only the left half of the box is shown: an equivalent fluid–air interface in the right half is not shown. The symbols are defined in the main text.

$\mathbf{v}$. For the viscoelastic stress $\mathbf{\Sigma}(\mathbf{r}, t)$, we assume zero gradient,

$$\mathbf{n}\cdot\nabla\mathbf{\Sigma} = 0, \tag{11}$$

in which $\mathbf{n}$ is the unit outward wall normal. For the phase field [43,44], we assume

$$\mathbf{n}\cdot\nabla\mu = 0, \tag{12}$$

$$\mathbf{n}\cdot\nabla\phi = \frac{-1}{\sqrt{2}\ell_\mu}\cos\theta\left(1-\phi^2\right). \tag{13}$$

In the absence of flow, the contact angle at which the fluid–air interface meets the walls of the flow cell is then given by the angle θ in the second of these equations: $\theta = 90^\circ$ gives a vertical interface, $\theta > 90^\circ$ gives an interface convex into the air, and $\theta < 90^\circ$ concave. In Ref. [29], we showed that while the steady state shape of the perturbed meniscus can depend on wetting angle, other quantitative predictions (e.g., the location of phase boundaries) are relatively robust to changes in θ.

In performing any simulation, we first take a rectangular slab of fluid centered horizontally in the simulation box of Fig. 2 (which, recall, shows only the left half of the area simulated), with length Λ in the vorticity direction. We then equilibrate the fluid–air coexistence in the absence of shear, to the contact angle just described. We then add a small perturbation to the interface's position $h(y)$ along the z direction, $h(y) \to h(y) + 10^{-8}\cos(\pi y/L_y)$. This is needed only when the interface is vertical, $\theta = 90^\circ$, but we add it for all values of θ, for consistency. The final steady state is independent of the small amplitude of the initial perturbation. It is also relatively robust against the shape of the added perturbation. In Sec. IV, the viscoelastic stress is initialized to lie on the stationary homogeneous constitutive curve for the shear rate in question, then we shear the fluid at that rate. In Sec. V, unless otherwise stated, we initialize with the corresponding 1D flow state which may be banded or homogeneous depending on the shear rate. In cases where the homogeneous state is metastable, we ensure that the initial state is banded by sweeping the shear rate from an appropriate starting value. We define the steady state interface displacement

$$d = \max(h(y)) - \min(h(y)), \tag{14}$$

with d_0 the value of this in a system without shear, noting that for $\theta = 90^\circ$, $d_0 = 0$.

The parameters pertaining to the model equations, flow geometry, boundary conditions, and imposed flow are summarized in Table I, along with the values to be used in our simulations. Details of our numerical methods can be found in Ref. [29]. In order to accurately reproduce the physics of the air–fluid coexistence, we require the air viscosity to be much smaller than the zero shear viscosity of the fluid (solvent and polymer combined), giving the condition $\eta_a \ll \eta_s + G\tau$. In the first part of our study (Sec. IV), we further require each constitutive model to have a monotonic constitutive curve, to rule out true bulk shear banding in the absence of any edge effects. For the Giesekus model, it is possible to obtain monotonic constitutive curves for values of $\eta_s \ll G\tau$. The condition $\eta_a \ll \eta_s + G\tau$ can then be met by adopting same air/solvent viscosity across the whole domain, $\eta_a \equiv \eta_s$, which is also numerically convenient. Accordingly, we follow this strategy in our simulations of the Giesekus model. For the Johnson–Segalman model, solvent viscosities η_s as large as 0.1 are needed to study marginally banded flows (Sec. V), and we can no longer equate η_a and η_s while also satisfying the condition $\eta_a \ll \eta_s + G\tau$. Therefore, in this case, we must simulate distinct air and solvent viscosities. To do so, we follow the method as described in detail in Ref. [29].

The numerical mesh size and time step have maximal values of $\delta_y = \delta_z = 0.0052$, $\delta_t = 0.006$. For each figure we have checked that the data are converged with respect to any further reduction of these numerical parameters.

In the phase diagrams of Figs. 6–9, 11, and 14 that follow, we display the numerically obtained threshold for edge instability as a black dashed line. This is calculated as follows. In the early time dynamics of the edge instability in any simulation run, the edge perturbation grows as $\sim e^{\omega t}$ (or decays, in the stable regime). By tracking this early time exponential growth (or decay), for a simulation at any coordinate pair of parameter values in any phase diagram, we extract the growth rate, ω, at that location in the phase diagram. By measuring this for a number of values of Γ/GL_y on either side of the threshold (at any fixed $\eta_s - \eta_c$ in Fig. 6, for example), we then obtain the point where $\omega = 0$ by linear interpolation. This black dashed line is thus determined independently from the information shown by the symbols in the phase diagrams,

TABLE I. Parameters; their dimensions in modulus [G], length [L], and time [T]; values used in our simulations; and notes. The first three parameters specify our choice of units. The second five are the key physical parameters to be varied in our study (four within each constitutive model). a and α set the dependences of σ and N_2 on $\dot{\gamma}$ and have been explored in earlier works [29]. The set from η_a to M does not affect the key physics, provided each assumes an appropriately large or small value; the final set are numerical parameters, which we ensure are converged to the appropriate small limit. Parameter values used in the simulations are as given in this table unless explicitly described otherwise. Johnson–Segalman (JS) and Giesekus (Gk).

Parameter	Description	Dimension	Value	Notes
L_y	Channel width	$[L]$	1.0	Unit of length
G	Polymer modulus	$[G]$	1.0	Unit of stress
τ	Polymer relaxation time	$[T]$	1.0	Unit of time
$\dot{\gamma}$	Applied shear rate	$[T]^{-1}$	$10^{-1} \rightarrow 10^2$	Important quantity to be varied
θ	Equilibrium contact angle	[1]	$30^{\circ} \rightarrow 150^{\circ}$	Important quantity to be varied
Γ	Surface tension	$[G][L]$	$0.01 \rightarrow 1.0$	Important quantity to be varied
η_s	Solvent viscosity (JS)	$[G][T]$	0.025 (strongly), 0.1 (marginally) banded	Small viscosity ratio $\eta_s/G\tau$
η_s	Solvent viscosity (Gk)	$[G][T]$	$0.006 \rightarrow 0.02$	Small viscosity ratio $\eta_s/G\tau$
a	Slip parameter (JS)	[1]	0.3	Sets dependencies $\Sigma_{xy}(\dot{\gamma})$, $N_2(\dot{\gamma})$
α	Anisotropy parameter (Gk)	[1]	0.8	Sets dependencies $\Sigma_{xy}(\dot{\gamma})$, $N_2(\dot{\gamma})$
η_a	Air viscosity (JS)	$[G][T]$	0.01	Small air viscosity $\eta_a/G\tau$
η_a	Air viscosity (Gk)	$[G][T]$	$\equiv\eta_s$	Small air viscosity $\eta_a/G\tau$
L_z	Channel length	$[L]$	20	Large aspect ratio L_z/L_y
Λ	midpoint sample length	$[L]$	16	Large air gap $(L_z - \Lambda)/L_y$
ℓ	Polymer microscopic length	$[L]$	0.01	Small microscopic length l/L_y
ℓ_μ	Air–polymer interface width	$[L]$	0.01	Small microscopic length ℓ_μ/L_y
M	Molecular mobility	$[L]^2[G]^{-1}[T]^{-1}$	0.0001	Rapid phase equilibration
δ_y	Numerical mesh size	$[L]$	Small	Converge δ_y/L_y until no dependence
δ_z	Numerical mesh size	$[L]$	Small	Converge δ_z/L_z until no dependence
δ_t	Numerical time step	$[T]$	Small	Converge δ_t/τ until no dependence

which pertain to the nonlinear states obtained in the limit of long time $t \rightarrow \infty$ in any simulation run.

IV. RESULTS: APPARENT BULK SHEAR BANDING INDUCED BY PRECURSORS TO EDGE FRACTURE

In this section, we explore in more detail the basic phenomenon announced in a recent Letter [1]: that even relatively modest precursors to an edge fracture instability of the fluid–air interface can induce apparent shear banding invading far into the bulk of a strongly shear thinning fluid. Importantly, this is true even if the underlying constitutive curve is monotone increasing, $d\sigma/d\dot{\gamma} > 0$, precluding true bulk banding in the absence of edge effects. Accordingly, we restrict our attention throughout this section to fluids for which the constitutive curve is indeed monotone increasing. As we shall discuss, the apparent shear banding invades progressively further into the fluid bulk for progressively flatter (but still monotone increasing) constitutive curves.

A set of constitutive curves computed within the Giesekus model for a fixed value of the anisotropy parameter α is shown in Fig. 3. (We fix $\alpha = 0.8$ throughout this section.) Although each curve is indeed monotone increasing, each has a relatively flat quasiplateau centered on a strain rate $\bar{\dot{\gamma}} \approx \sqrt{10}$. The flatness of this plateau will prove an important quantity in what follows. We shall quantify it via the plateau width,

$$n = \log_{10}(\dot{\gamma}_h/\dot{\gamma}_l), \tag{15}$$

determined by the shear rates $\dot{\gamma}_h$, $\dot{\gamma}_l$ at the extrema of the plateau, corresponding to $\pm 5\%$ of the stress at the flattest point. In what follows, we shall report results both in terms of the plateau width, n, and the solvent viscosity, $\eta_s - \eta_c$ (where $\eta_c = 0.005\,918$ is the value of η_s below which the constitutive curve is nonmonotonic, for $\alpha = 0.8$). We note that n is directly set by η_s and is more directly measurable in any experiment. Stronger shear thinning corresponds to lower values of η_s and larger values of n.

Having discussed the homogeneous (0D) bulk constitutive curves, we now present the results of our fully 2D simulations. Throughout this section, we fix the value of the wetting angle, $\theta = 90°$. Important parameters to be varied are then the solvent viscosity, η_s, which sets the shape of the constitutive curve in the way that we have just discussed, the imposed shear rate, $\bar{\dot{\gamma}}$, and the surface tension of the fluid–air interface, Γ. We focus on values of the surface tension for which the fluid–air interface is modestly disturbed by flow, giving partial edge fracture, as in the simulation snapshots of Fig. 4. In particular, we avoid the regime of full edge fracture in which the interface loses its integrity altogether and the fluid completely dewets the wall. (Typical values of $\Gamma = \Gamma/GL_y$ are 0.001–0.1 for synthetic polymers and 0.1–10.0 for DNA solutions [2,33,34,45–48].)

Although such modest edge disturbances may in themselves go unnoticed experimentally, they are nonetheless capable of causing a much more dramatic quasibulk shear banding phenomenon. This is increasingly evident in successive snapshots downward in Fig. 4, which correspond to simulations performed for successive constitutive curves downward in Fig. 3, at a fixed shear rate $\bar{\dot{\gamma}} = 4.7$ in the quasiplateau regime in each case, for a surface tension $\Gamma = 0.16$. Indeed, an apparent shear banding phenomenon that is strongly localized near the fluid–air interface for a relatively steep constitutive curve invades progressively further along the vorticity direction into the bulk, away from the fluid–air interface, for progressively flatter constitutive curves. The corresponding velocity profile across the flow-gradient direction y at the cell center, $z = 8$ (Fig. 5, right) accordingly becomes increasingly banded. (We denote by $z = 0$ the position of the left hand fluid–air interface at the start of the simulation run.)

To quantify the degree to which the flow is shear banded across the flow-gradient direction y at any distance z away from the fluid–air interface, we define

$$\Delta_{\dot{\gamma}}(z) = [\dot{\gamma}_{\max}(z) - \dot{\gamma}_{\min}(z)]/\bar{\dot{\gamma}}, \tag{16}$$

with $\dot{\gamma}_{\max}(z)$ the maximum shear rate at any point across y at fixed z, and $\dot{\gamma}_{\min}$ the counterpart minimum value. $\bar{\dot{\gamma}}$ is the gap-averaged shear rate. By inspecting many profiles, we adopt $\Delta^c_{\dot{\gamma}} = 0.15$ as the minimum threshold value of this measure to give visually apparent banding in the velocity profile. Plots of $\Delta_{\dot{\gamma}}$ as a function of distance z into the bulk are shown in Fig. 5 (left). As can be seen, visually apparent banding persists right to the center of the flow cell for the flattest constitutive curves in Fig. 3.

So far, we have shown that the degree to which disturbances at the fluid–air interface can induce apparent shear banding into the fluid bulk increases with increasing shear thinning in the underlying constitutive curve. In doing so, we have kept the surface tension Γ of the fluid–air interface fixed, and considered a single value of the imposed shear rate, $\bar{\dot{\gamma}}$, near the flattest part of the constitutive curve. We now explore the effects on this phenomenon of also (first) varying the surface tension, Γ, and then (second) the imposed shear rate, $\bar{\dot{\gamma}}$.

Phase diagrams are shown in Fig. 6 of the degree of disturbance of the fluid–air interface (top) and of apparent shear banding at the midpoint of the fluid bulk (bottom) in the plane of surface tension, Γ, and degree of shear thinning in the constitutive curve, n, again for a fixed value of the imposed shear rate, $\bar{\dot{\gamma}}$, near the flattest part of the constitutive curve. A horizontal slice across this phase diagram accordingly spans a suite of constitutive curves with varying degrees of shear thinning, with lower values of n right to left giving stronger shear thinning. For a fixed value of surface tension, the degree of edge disturbance and of shear banding at the cell midpoint both increase with increasing shear thinning from right to left. For a fixed degree of shear thinning, the same quantities increase with decreasing surface tension, from top to bottom.

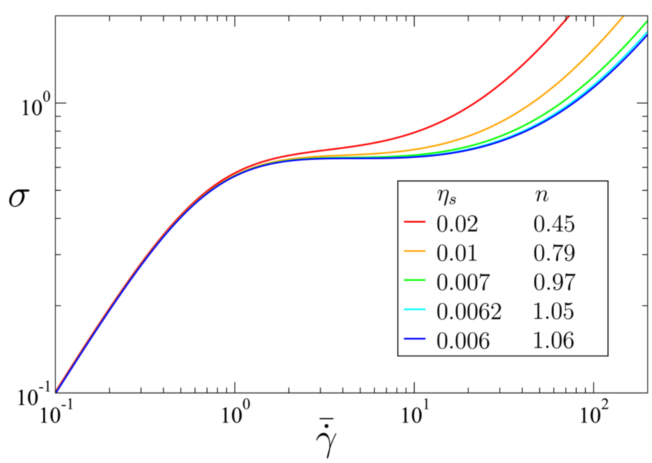

FIG. 3. Constitutive curves of shear stress as a function of shear rate for stationary homogeneous shear flow. All curves are computed in the Giesekus model for a fixed value of the anisotropy parameter, $\alpha = 0.8$. All curves are monotone increasing, but increasingly flatter curves downward pertain to increasingly more shear thinning fluids, with Newtonian viscosities $\eta_s = 0.02$, 0.01, 0.007, 0.0062, and 0.006. The caption also shows the equivalent plateau width n [see Eq. (15) for definition].

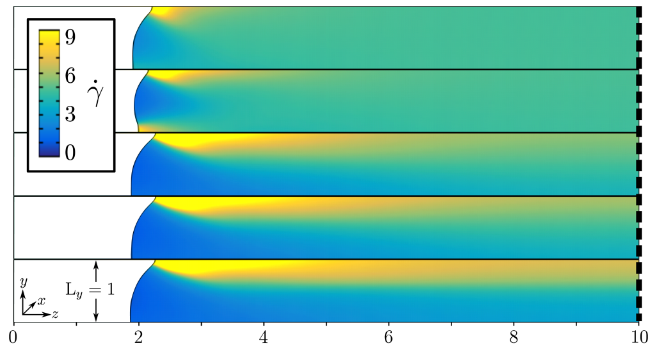

FIG. 4. Simulation snapshots showing the frame invariant local shear rate, $\dot{\gamma}(\mathbf{r}) = \sqrt{2\mathbf{D}(\mathbf{r}):\mathbf{D}(\mathbf{r})}$, at an imposed shear rate $\bar{\dot{\gamma}} = 4.7$, in the quasiplateau regime of the constitutive curve, for a fluid–air interfacial tension $\Gamma = 0.16$. Snapshots downward correspond to constitutive curves downward in Fig. 3. An apparent shear banding phenomenon invades further into the fluid bulk for progressively flatter constitutive curves. $\theta = 90°$.

Phase diagrams of the same quantities are again shown in Fig. 7 but now in the plane of surface tension, Γ, and imposed shear rate, $\bar{\dot{\gamma}}$, for a fixed degree of shear thinning in the constitutive curve, n. A horizontal slice across this phase diagram accordingly spans a range of imposed shear rates for one particular constitutive curve with a fixed degree of shear thinning. For a fixed value of surface tension less than about 0.8, the degree of edge disturbance and of shear banding at the cell midpoint are noticeable for values of the shear rate in the quasiplateau regime of the constitutive curve. For any fixed value of shear rate on this quasiplateau, the same quantities increase with decreasing surface tension of the fluid–air interface, top to bottom down the phase diagram.

How can we understand this apparent shear banding phenomenon? As discussed in Ref. [29], the physical mechanism of the instability that leads to significant disturbances of the fluid–air interface involves a perturbation $\delta\Sigma_{xy}(y, z)$ to the shear stress field across the flow-gradient direction y, which gradually decays as a function of the distance z away from fluid–air interface. This leads to a corresponding disturbance $\delta\dot{\gamma}(y, z)$ in the shear rate field, by an amount that scales as the inverse slope of the constitutive curve. For a strongly shear thinning fluid, therefore, even a relatively modest disturbance to the shear stress creates a large disturbance of the shear rate, causing apparent shear banding.

A related question is then how these stress and shear rate heterogeneities associated with disturbances of the fluid–air interface compare with those associated with the geometries

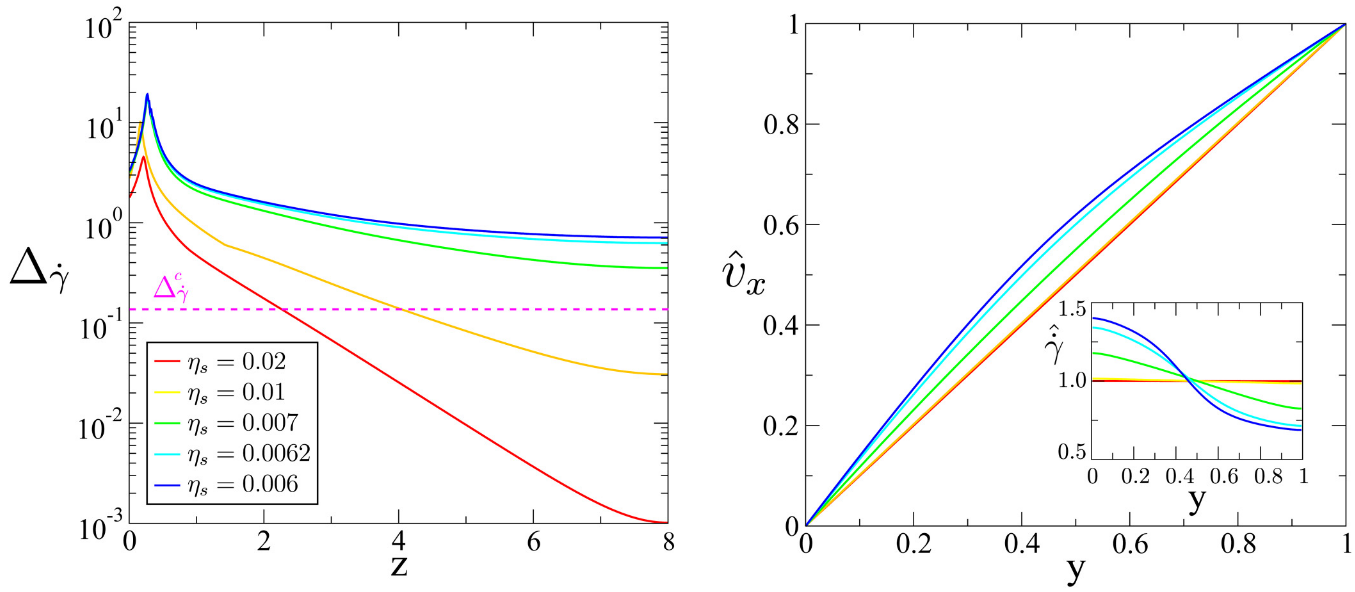

FIG. 5. Left: degree of apparent shear banding across the flow-gradient direction y as a function of distance z along the vorticity direction away from the fluid–air interface, into the bulk. Curves upward correspond to increasingly flatter constitutive curves in Fig. 3. Dashed magenta line indicates the value of the degree of banding above which banding is indeed obviously apparent in the velocity profiles. Right: normalized velocity profiles $\hat{v}_x(y)$ across the cell midpoint $z = 8$ (black dashed line in Fig. 4). Increasingly shear banded profiles correspond to increasingly flatter constitutive curves in Fig. 3. Inset: normalized local shear rate $\hat{\dot\gamma}(y)$. $\bar{\dot\gamma} = 4.7$, $\Gamma = 0.16$, $\theta = 90°$.

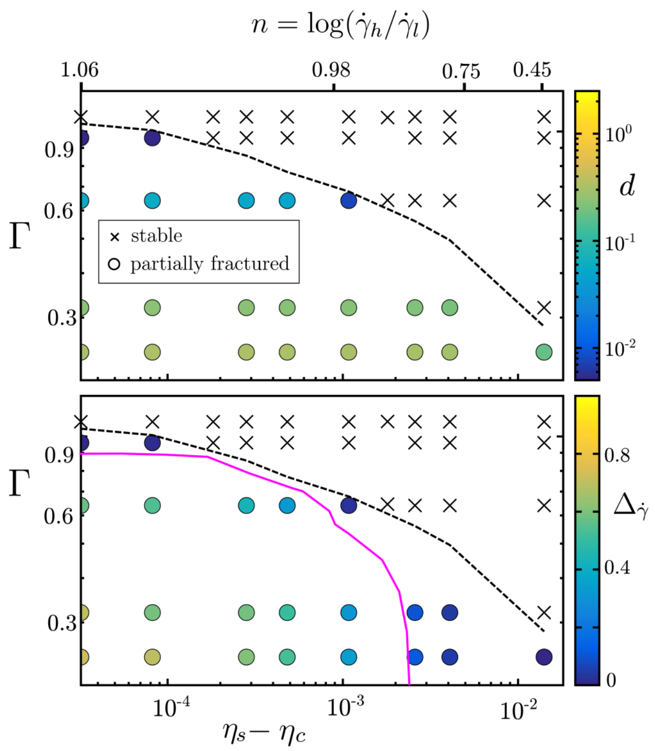

FIG. 6. Top: phase diagram showing the degree of disturbance of the air–fluid interface, d [as defined in Eq. (14)]. Black dashed line: onset of positive eigenvalue for edge disturbance, as determined numerically. Bottom: phase diagram of the degree of shear banding [as defined in Eq. (16)] at the cell midpoint, $\Delta_{\dot\gamma}(z = 8.0)$. Magenta solid line: contour $\Delta^c_{\dot\gamma} = 0.15$, which we take as the threshold for visually apparent banding, as obtained from a linear interpolation of the data. Both phase diagrams are shown in the plane of surface tension (ordinate) and an abscissa characterizing the degree of shear thinning in the constitutive curve. The bottom abscissa shows the value of the Newtonian viscosity, relative to that at which the constitutive curve develops a slope of zero, $\eta_s - \eta_c$. This decreases with increasing shear thinning right to left. The top abscissa shows the number of decades spanned by the quasiplateau in the constitutive curve, n. This increases with increasing shear thinning right to left. Imposed shear rate $\bar{\dot\gamma} = 4.7$, $\theta = 90°$.

of typical flow cells. This is especially pertinent in light of the results of Ref. [49] which demonstrated that stress gradients (originating from geometry) can cause shear banding phenomena in fluids that are described by a monotonic underlying constitutive curve.

Figure 8 shows phase diagrams of the degree of stress heterogeneity across the flow-gradient direction y caused by disturbances in the fluid–air interface, at distances of $z = 4.0$ (top) and $z = 8.0$ (bottom) into the fluid. For reference, the colorbar additionally shows the level of stress heterogeneity that would instead arise from device geometry for cone–plate cells of various cone angles. Given that typical cone angles are about 0.5°–1°, the stress heterogeneity and corresponding apparent shear banding that we observe clearly exceed those arising from typical cell geometries.

V. EDGE FRACTURE INDUCED BY SHEAR BANDING

A. Marginally nonmonotonic constitutive curve

We consider now a fluid with a nonmonotonic constitutive curve, giving a bulk flow that is shear banded over some range of strain rates (even in the absence of any edge effects). In particular, we seek to appraise using our simulations the analytical predictions of Skorski and Olmsted [2]: that shear banding in the fluid bulk can induce full edge fracture at the fluid–air interface, for some values of the surface tension and imposed shear rate. It should be noted that the work in Ref. [2] did not perform a dynamic calculation, nor did it consider the effect of secondary flows. We start by considering a constitutive curve that is only marginally nonmonotonic, giving a relatively small jump in the shear rate across the interface between the shear bands, before discussing in Subsection V B below a more highly nonmonotonic curve, giving a larger jump.

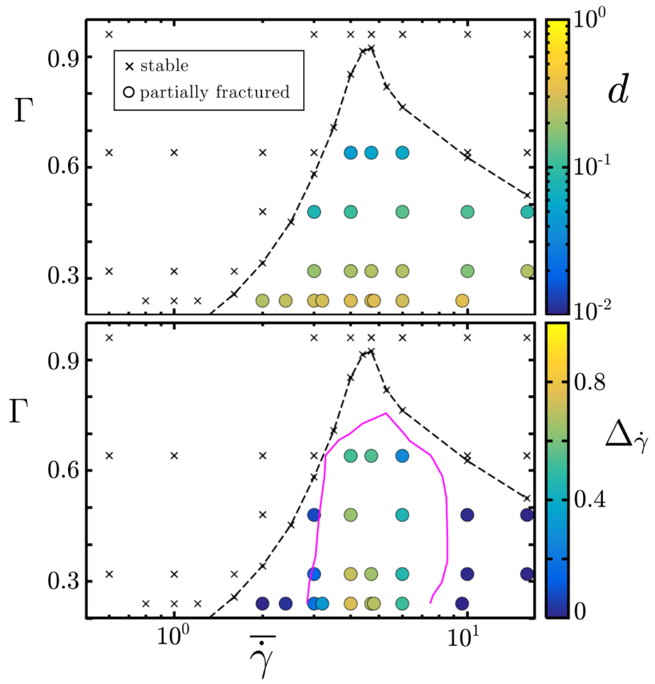

FIG. 7. Top: phase diagram of the degree of disturbance of the air–fluid interface, d [as defined in Eq. (14)]. Bottom: phase diagram of the degree of shear banding [as defined in Eq. (16)] at the cell midpoint, $\Delta_{\dot{\gamma}}(z = 8.0)$. Magenta solid line: contour $\Delta^c_{\dot{\gamma}} = 0.15$, as obtained from a linear interpolation of the data, which we take as the threshold for visually observable shear banding. In both diagrams, the numerically determined onset of the positive eigenvalue for edge disturbance is shown (black dashed line). Both phase diagrams are shown in the plane of surface tension (ordinate) and imposed shear rate (abscissa). Both pertain to a constitutive curve with a degree of shear thinning prescribed by a fixed value of Newtonian viscosity $\eta_s = 0.006$, with a quasiplateau spanning $n = 1.06$ decades. $\theta = 90°$.

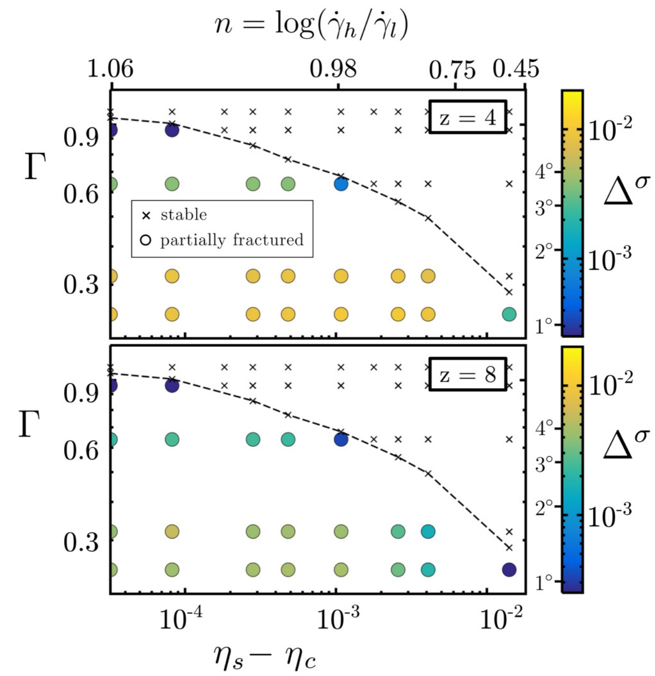

FIG. 8. Phase diagrams showing the degree of shear stress heterogeneity $\Delta^\sigma = \sigma_{\max}/\sigma_{\min} - 1$ that arises due to the disturbance of the fluid–air interface at a distance of $z = 4.0$ (top) and 8.0 (bottom) into the fluid bulk. For reference, the colorbars are additionally marked with the degree of stress heterogeneity that would arise in a cone and plate device with a cone angle of 1°, 2°, 3°, or 4°. Imposed shear rate $\bar{\dot{\gamma}} = 4.7$, $\theta = 90°$.

A marginally nonmonotonic constitutive curve is accordingly shown in Fig. 9 (top). The corresponding second normal stress as a function of shear rate is shown on the right hand axis. These two curves pertain to a state of stationary homogeneous (0D) shear flow. In the regime of negative constitutive slope, $d\sigma/d\dot{\gamma} < 0$, an initially homogeneous flow is linearly unstable to the formation of shear bands. The shear rates delineating this regime are shown by vertical dotted lines in Fig. 9. The steady flow state, computed within a 1D calculation that now allows shear banding (but still ignores edge effects), is then shear banded. This leads to a plateau in the steady state flow curve (red circles). The shear rates delineating this regime are shown by vertical solid lines. Between the dotted and solid vertical lines, an initially homogeneous flow is metastable to the formation of shear bands.

Having discussed these 0D and 1D states, we now discuss our fully 2D simulations, in which a sheared slab of fluid coexists with the outside air, separated by a fluid–air interface. These simulations allow a study of any edge fracturelike disturbances at that fluid–air interface, as well as any shear banding within the fluid bulk.

A colormap showing the degree of disturbance of the fluid–air interface as a function of the surface tension of that interface, Γ, and the imposed shear rate, $\bar{\dot{\gamma}}$, can be found in Fig. 9 (bottom). Outside the regime where the bulk flow is shear banded, the interface remains undisturbed at high values of the surface tension but is always disturbed at lower values of the surface tension. The red dashed lines show the analytical prediction of Hemingway and Fielding [28,29] for the onset of a linear instability to these disturbances—i.e., for the onset of partial edge fracture—for this case of a homogeneous (unbanded) bulk shear flow. This was derived in the limit of low strain rates, where it indeed agrees well with the onset of partial edge fracture in our simulations (black dashed lines).

Consider now imposed shear rates inside the shear banding regime, within the vertical solid lines. Here, the fluid–air interface is always disturbed to some extent, although by an amount that diminishes with increasing surface tension. This is consistent with the work of Skorski and Olmsted [2], who noted that an edge disturbance is an inevitable consequence of force balance for a shear banded flow, due to the jump in second normal stress across the interface between the bands.

Having explored in Fig. 9 the degree of edge disturbance, d, as a function of surface tension, Γ, and imposed shear rate, $\bar{\dot{\gamma}}$, we show in Fig. 10 a collection of horizontal slices across this plane, now plotting d as a function of $\bar{\dot{\gamma}}$ for several fixed values of Γ. Consistent with the above discussion, the interface is always disturbed to some degree inside the shear banding regime. Outside the banding regime, the interface is undisturbed for large values of surface tension, but disturbed for smaller values.

A noticeable feature of Fig. 10 is that, for several values of the surface tension, the degree of edge disturbance varies smoothly across the critical shear rate that marks the onset of bulk shear banding. This is *a priori* surprising: within a 1D

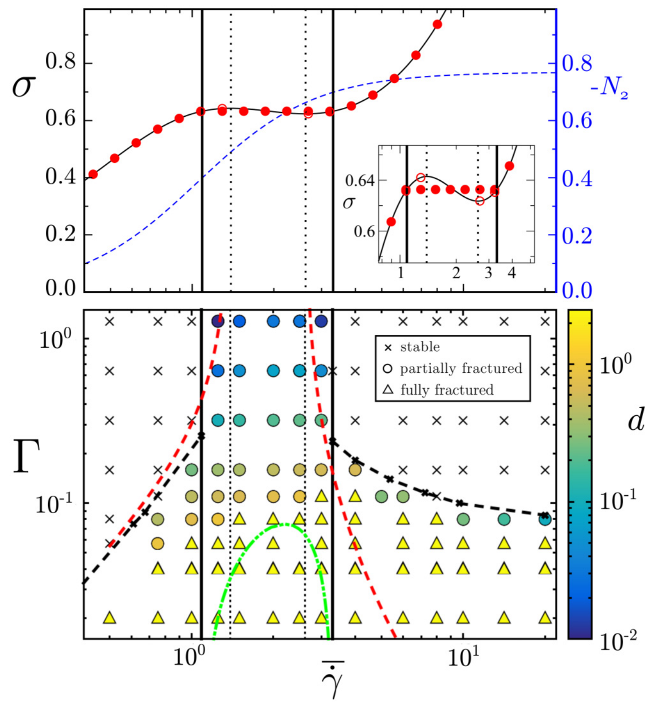

FIG. 9. Top: Homogeneous (0D) constitutive curve (black curve) and steady state flow curve computed in a 1D simulation (red solid circles). Inset shows the same data, zoomed to focus on the shear banding regime. Open red circles denote metastable states of homogeneous shear flow. Dashed blue line shows (minus) the second normal stress, $-N_2$. Bottom: Colormap of degree of disturbance to the fluid–air interface, d, in the plane of the surface tension of that interface, Γ, and the imposed shear rate, $\bar{\dot{\gamma}}$. Black dashed lines denote the numerically determined onset of edge disturbance, red dashed line marks the threshold for instability as determined via linear stability analysis, and green dashed-dotted line shows the analytical prediction of Ref. [2]. The Johnson–Segalman model, $\eta_s = 0.1$, $\theta = 90°$.

calculation, free of edge effects, the bulk flow undergoes a qualitative transition from unbanded to banded across that critical shear rate. One might, therefore, expect very different levels of edge disturbance once the fluid–air interface is accounted for in 2D. The resolution to this puzzle lies in recognizing that the edge disturbances actually in turn modify the bulk state, at least for some distance away from the fluid–air

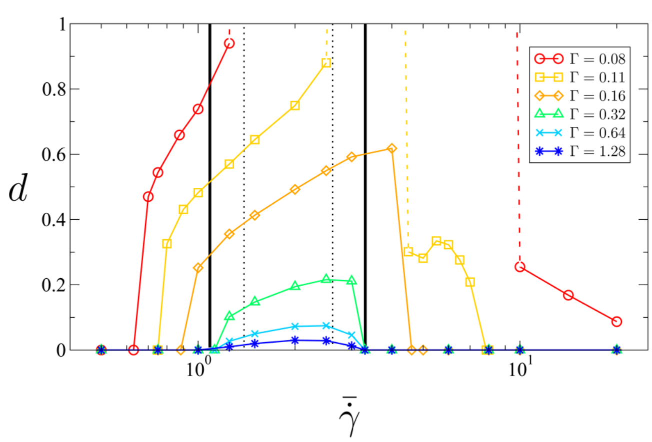

FIG. 10. Horizontal slices across the colormap of Fig. 9 (bottom) showing the degree of disturbance to the fluid–air interface, d, as a function of the imposed shear rate, $\bar{\dot{\gamma}}$, for several values of the surface tension of the fluid–air interface, Γ.

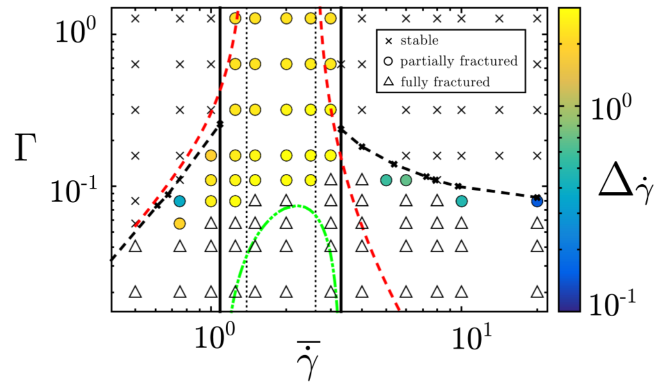

FIG. 11. Colormap showing the degree of shear banding $\Delta_{\dot{\gamma}}$ [as defined in Eq. (16)], measured at a position $z = 1$ into the bulk away from the fluid–air interface, shown in the same plane of surface tension and shear rate as in Fig. 9. Open triangles denote fully edge fractured states, in which $\Delta_{\dot{\gamma}}$ cannot be reliably measured. Black dashed lines denote the numerically determined onset of edge disturbance. Red dashed line marks the threshold for instability as determined via linear stability analysis. Green dashed-dotted line shows the analytical prediction of Ref. [2]. The Johnson–Segalman model, $\eta_s = 0.1$, $\theta = 90°$.

interface into the fluid: as seen for a shear rate $\dot{\gamma} = 1.0$ and surface tension values $\Gamma = 0.08, 0.16$ in Fig. 12, the flow becomes quasibanded a little way into the bulk, even at a shear rate a little below that for which a purely 1D calculation (without a fluid–air interface) would predict banding. This is simply another (albeit relatively mild) manifestation of the phenomenon discussed in Sec. IV above. A colormap of the degree to which the flow is shear banded a little distance ($z = 1$) into the fluid away from the fluid–air interface indeed confirms this (see Fig. 11).

As discussed above, at low values of surface tension the fluid–air interface always becomes fully fractured. Skorksi and Olmsted [2] predicted the location of the transition from partial to full fracture for a shear banded state by arguing that, as the relative fraction of the rheometer gap taken up by each band changes with the imposed shear rate, one of the bands can develop a width that is unable to support the meniscus curvatures demanded by the second normal stress balance, leading to full fracture. Their prediction is marked by a green dashed line in Figs. 9 and 11. The regime in which our simulations display full fracture is shown by yellow triangles. The agreement between the analytical predictions and our simulations is at best fair, possibly because Skorski and Olmsted assumed an initial "base" state with no secondary flows. Secondary flows nonetheless inevitably arise, as seen in Fig. 13.

B. Highly nonmonotonic constitutive curve

We consider finally a fluid with a highly nonmonotonic constitutive curve, giving a large jump in shear rate across the interface between the bands. The top two panels of Fig. 14 show results for this case in the same format as the two panels of Fig. 9 for a marginally nonmonotonic curve. Many of the same features are apparent. Outside the regime where the bulk flow is shear banded, the fluid–air interface remains undisturbed at high values of the surface tension, but is disturbed at lower values. At low shear rates, the numerically

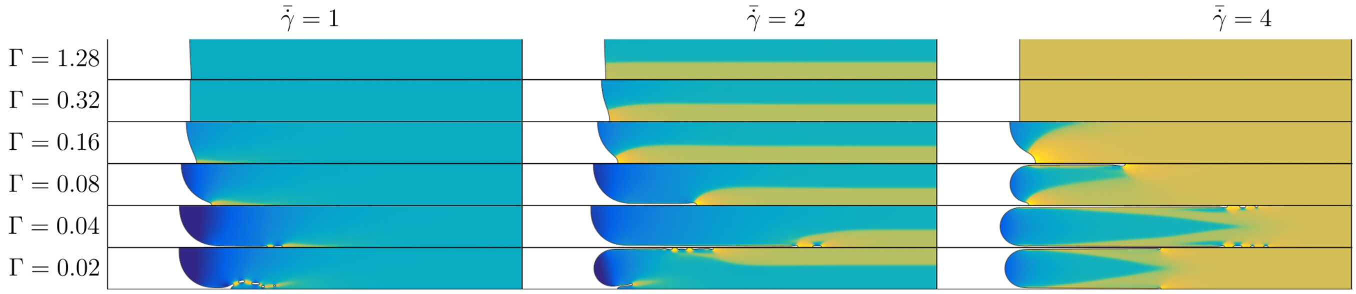

FIG. 12. Simulation snapshots showing the locally invariant shear, rate $\dot{\gamma}(\mathbf{r}) = \sqrt{2\mathbf{D}(\mathbf{r}):\mathbf{D}(\mathbf{r})}$, for the case of a marginally nonmonotonic constitutive curve. Applied shear rate $\bar{\dot{\gamma}} = 1.0, 2.0, 4.0$ (left to right) and surface tension $\Gamma = 0.02, 0.04, 0.08, 0.16, 0.32, 1.28$ (bottom to top). The Johnson–Segalman model, $\eta_s = 0.1$, $\theta = 90°$.

observed transition from an undisturbed to a disturbed fluid–air interface (black dashed line) agrees well with the analytical prediction of Hemingway and Fielding, given a homogeneous (unbanded) bulk flow (red dashed line) [28,29].

In contrast, when the bulk flow is shear banded the fluid–air interface is always disturbed to some extent, although by an amount that diminishes with increasing surface tension. This is again consistent with the argument of Skorski and Olmsted, that a shear banded state must always have a disturbed interface on account of the second normal stress jump across the interface between the bands [2]. Snapshots of the locally invariant shear rate for a fixed shear rate $\bar{\dot{\gamma}} = 6.0$ inside the shear banding regime are shown in Fig. 15, with the surface tension increasing in subpanels upward.

At low values of surface tension, the fluid–air interface always becomes fully fractured, as shown by the yellow triangles in Fig. 14. The prediction of Skorski and Olmsted [2] for the onset of full fracture in the shear banding regime is marked by a green dashed line in Fig. 14. It shows fair agreement with our simulations—which is perhaps mainly fortuitous, given the poorer agreement in Fig. 9 and (as we shall shortly discuss) Fig. 16.

In a narrow window of shear rates at the lower end of the regime where shear banding is expected, the bulk flow is unexpectedly homogeneous, and the fluid–air interface is accordingly unexpectedly undisturbed. See the black crosses for an imposed shear rate $\bar{\dot{\gamma}} = 0.5$ and surface tension $\Gamma \geq 0.08$ in Fig. 14 (middle). For such shear rates, the width of the low shear band itself would be smaller than the finite thickness of the interface itself. The flow therefore remains unbanded. Simulations for a much smaller value of the parameter that sets the thickness of the interface between the shear bands would be shear banded and would presumably then also have a disturbed fluid–air interface.

The bottom panel of Fig. 14 shows results exactly as in the middle panel, but now for an initial condition that, in the two windows of shear rate between the solid and dotted vertical lines, is one of metastable homogeneous shear. At relatively high values of surface tension in these metastable regimes, the bulk flow remains unbanded throughout the entire simulation. The threshold for the onset of a disturbed fluid–air interface is then that which pertains to an unbanded bulk, as given by the red dashed line, following the criterion of Hemingway and Fielding [28,29]. (Recall that this criterion is only valid at low shear rates.) The metastable states of homogeneous shear accordingly remain unbanded at high enough surface tension, and with an undisturbed fluid–air interface, leading to black crosses in Fig. 14 (bottom). For a shear banded initial condition, in contrast, the fluid–air interface must be disturbed [2], indeed leading to blue or turquoise circles in Fig. 14 (middle) in place of the black crosses in the bottom panel.

C. Effect of wetting angle

Recall that the angle subtended by the fluid–air interface where it meets the walls of the flow cell defines the wetting angle. The equilibrium value of this quantity in the absence of any imposed shear, θ, is set by the boundary conditions for the Cahn–Hilliard sector of the dynamics [Eq. (13)]. All simulations reported so far have taken a value $\theta = 90°$, such that the interface is vertical and flat in the absence of shear. We consider finally the effect of varying θ. For values of $\theta \neq 90°$, the fluid–air interface is either concave or convex even in the absence of shear, with a degree of bowing d_0. Accordingly, we subtract this quantity d_0, from the degree of interfacial bowing in the presence of shear, d, to get the degree of interfacial disturbance caused by shear, $d - d_0$.

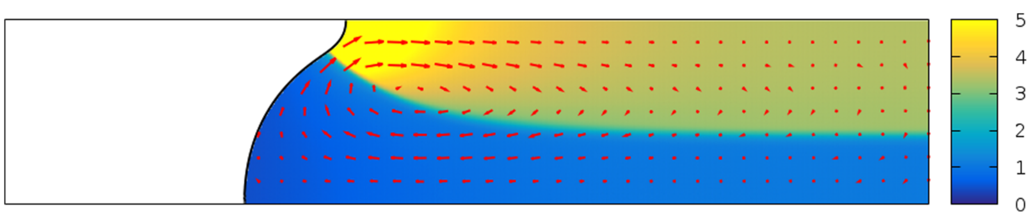

FIG. 13. Colormap of the frame invariant shear rate, $\dot{\gamma}(\mathbf{r}) = \sqrt{2\mathbf{D}(\mathbf{r}):\mathbf{D}(\mathbf{r})}$, showing secondary flows (red arrows) near the fluid–air interface. The Johnson–Segalman model, $\bar{\dot{\gamma}} = 2.5$, $\Gamma = 0.16$, $\eta_s = 0.1$, $L_z = 10$, $\Lambda = 7$, $\theta = 90°$.

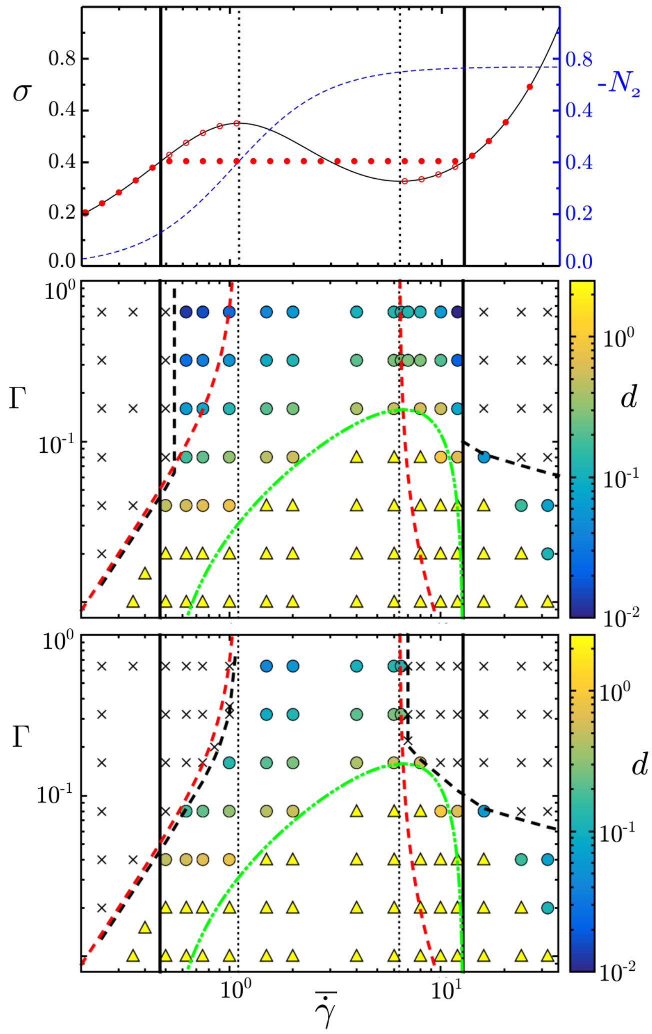

FIG. 14. Top: Homogeneous (0D) constitutive curve (black curve) and steady state flow curve computed in a 1D simulation (red solid circles). Open red circles denote metastable states of homogeneous shear flow. Dashed blue line shows (minus) the second normal stress, $-N_2$. Middle: Colormap of degree of disturbance to the fluid–air interface d [as defined in Eq. (14)], in the plane of the surface tension of that interface, Γ, and the imposed shear rate, $\bar{\dot{\gamma}}$. Bottom: Same as in middle figure, but for an initial condition of metastable homogeneous shear in the window of shear rates between the solid and dashed vertical lines. Black dashed lines denote the numerically determined onset of edge disturbance, red dashed line marks the threshold for instability as determined via linear stability analysis, and green dashed-dotted line shows the analytical prediction of Ref. [2]. The Johnson–Segalman model, $\eta_s = 0.025$, $\theta = 90°$.

Colormaps of this quantity are shown as a function of wetting angle, θ, and imposed shear rate, $\bar{\dot{\gamma}}$, for two different values of the surface tension of the fluid–air interface, Γ, in Fig. 16 (middle and bottom). Values of $\theta, \bar{\dot{\gamma}}$ for which the fluid–air interface is found to be partially edge fractured in our simulations are shown by circles. Values for which full edge fracture occurs are shown by triangles. The transition between partially and fully edge fractured states as predicted analytically by Skorski and Olmsted [2] is shown by the green dashed lines.

The arguments of [2] rested on the shape of the fluid–air interface determined by force balance, taking into account the jump in N_2 across the interface between the shear bands, the relative widths of the low and high shear bands (which is

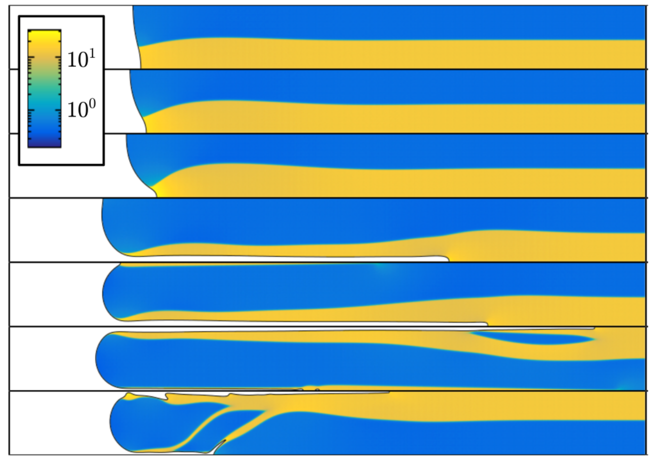

FIG. 15. Simulation snapshots showing the locally invariant shear rate, $\dot{\gamma}(\mathbf{r}) = \sqrt{2\mathbf{D}(\mathbf{r}):\mathbf{D}(\mathbf{r})}$, for the case of a highly nonmonotonic constitutive curve. Applied shear rate $\bar{\dot{\gamma}} = 6.0$ with a surface tension $\Gamma = 0.01, 0.02, 0.04, 0.08, 0.16, 0.32, 0.64$ (bottom to top). The Johnson–Segalman model, $\eta_s = 0.025$, $\theta = 90°$.

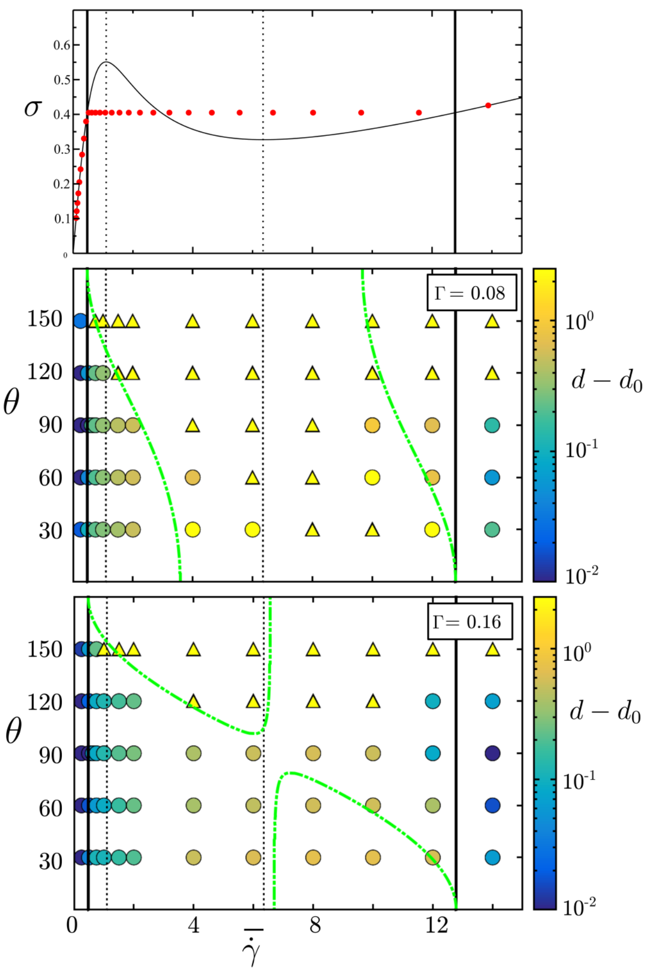

FIG. 16. Homogeneous (0D) constitutive curve (black curve) and steady state flow curve computed in a 1D simulation (red solid circles). Middle: Colormap of degree of disturbance to the fluid–air interface, $d - d_0$, in the plane of the wetting angle, θ, and the imposed shear rate, $\bar{\dot{\gamma}}$, for a fixed value of the surface tension $\Gamma = 0.08$. Bottom: Corresponding colormap for $\Gamma = 0.16$. Green dashed-dotted line shows the analytical prediction of Ref. [2]. The Johnson–Segalman model, $\eta_s = 0.025$.

set by $\bar{\dot{\gamma}}$), and the wetting angle at the walls. As a direct result, the transition lines predicted in that work show the symmetry apparent in Fig. 16 in the plane of θ and $\bar{\dot{\gamma}}$. The results of our numerical simulations do not obey even these basic symmetries, however. This discrepancy again presumably arises due to the presence of secondary flows near the fluid–air interface, which lead these basic assumptions of Skorski and Olmsted to break down.

VI. CONCLUSIONS

In this work, we have studied the interplay between shear banding and edge fracture in complex fluids, mapping out phase diagrams of the levels of edge disturbance and bulk (or quasibulk) shear banding as a function of the surface tension of the fluid–air interface, the wetting angle at the walls of the flow cell, and the imposed shear rate. We have explored, in particular, the basic result announced in Ref. [1]: that precursors to edge fracture can induce quasibulk shear banding, even in fluids for which the underlying constitutive curve is monotonic, such that a bulk flow is predicted to be unbanded in the absence of edge effects. We have also appraised analytical predictions, made within some assumptions, that shear banding can induce edge fracture [2]. Our simulations have shown that this basic prediction remains valid but that the phase boundaries are qualitatively modified due to a breakdown of those assumptions.

As discussed above, an outstanding question is whether the underlying constitutive curve of monodisperse linear entangled polymers is monotonic or nonmonotonic, and so whether a steady applied shear flow should be homogeneous or shear banded. Experimental evidence for shear banding is mixed and controversial [32–34], with edge fracture often discussed as a confounding factor [14,34–37]. It would be interesting to reappraise these existing experiments data in the light of our new theoretical findings and to perform new experiments aimed specifically at studying the interplay between shear banding and edge fracture described here.

We discuss finally some shortcomings of our work that should be rectified in future studies. We have assumed throughout a base state corresponding to a state of time-independent shear flow (whether banded or unbanded). Edge fracture is also widely seen in transient flows such as shear startup. Future theoretical work should, therefore, consider the effects of a time-dependent base state on the phenomena reported here. We have further considered the limit of planar Couette flow, arguing that this geometry provides a good approximation to cylindrical Couette, cone–plate or plate–plate flow. We have thereby neglected the stress heterogeneity, streamline curvature, and secondary bulk flows that can arise in such devices. Future simulation studies should take these effects properly into account. We have also ignored wall slip, which occurs widely in complex fluids. Future theoretical studies should consider the relative dominance of and/or interplay between edge fracture and wall slip. Finally, we have ignored inertia, which may be relevant to the nonlinear dynamics of edge fracture, and should be considered in future theoretical work.

ACKNOWLEDGMENTS

The research leading to these results has received funding from the European Research Council under the EU's 7th Framework Programme (No. FP7/2007-2013)/ERC (Grant No. 279365).

REFERENCES

[1] Hemingway, E. J., and S. M. Fielding, "Edge-induced shear banding in entangled polymeric fluids," Phys. Rev. Lett. **120**, 138002 (2018).
[2] Skorski, S., and P. D. Olmsted, "Loss of solutions in shear banding fluids driven by second normal stress differences," J. Rheol. **55**, 1219–1246 (2011).
[3] Divoux, T., M. A. Fardin, S. Manneville, and S. Lerouge, "Shear banding of complex fluids," Annu. Rev. Fluid Mech. **48**, 81–103 (2016).
[4] Olmsted, P. D., "Perspectives on shear banding in complex fluids," Rheol. Acta **47**, 283–300 (2008).
[5] Manneville, S., "Recent experimental probes of shear banding," Rheol. Acta **47**, 301–318 (2008).
[6] Fielding, S. M., "Shear banding in soft glassy materials," Rep. Prog. Phys. **77**, 102601 (2014).
[7] Britton, M. M., and P. T. Callaghan, "Two-phase shear band structures at uniform stress," Phys. Rev. Lett. **78**, 4930–4933 (1997).
[8] Salmon, J.-B., S. Manneville, and A. Colin, "Shear banding in a lyotropic lamellar phase. I. Time-averaged velocity profiles," Phys. Rev. E **68**, 051503 (2003).
[9] Manneville, S., A. Colin, G. Waton, and F. Schosseler, "Wall slip, shear banding, and instability in the flow of a triblock copolymer micellar solution," Phys. Rev. E **75**, 061502 (2007).
[10] Michel, E., J. Appell, F. Molino, J. Kieffer, and G. Porte, "Unstable flow and nonmonotonic flow curves of transient networks," J. Rheol. **45**, 1465–1477 (2001).
[11] Rogers, S. A., D. Vlassopoulos, and P. T. Callaghan, "Aging, yielding, and shear banding in soft colloidal glasses," Phys. Rev. Lett. **100**, 128304 (2008).
[12] Martin, J. D., and Y. T. Hu, "Transient and steady-state shear banding in aging soft glassy materials," Soft Matter **8**, 6940–6949 (2012).
[13] Coussot, P., J. S. Raynaud, F. Bertrand, P. Moucheront, J. P. Guilbaud, H. T. Huynh, S. Jarny, and D. Lesueur, "Coexistence of liquid and solid phases in flowing soft-glassy materials," Phys. Rev. Lett. **88**, 218301 (2002).
[14] Li, Y., M. Hu, G. B. McKenna, C. J. Dimitriou, G. H. McKinley, R. M. Mick, D. C. Venerus, and L. A. Archer, "Flow field visualization of entangled polybutadiene solutions under nonlinear viscoelastic flow conditions," J. Rheol. **57**, 1411–1428 (2013).
[15] Wang, S.-Q., G. Liu, S. Cheng, P. E. Boukany, Y. Wang, and X. Li, "Letter to the editor: Sufficiently entangled polymers do show shear strain localization at high enough Weissenberg numbers," J. Rheol. **58**, 1059–1069 (2014).
[16] Wang, S.-Q., S. Ravindranath, and P. E. Boukany, "Homogeneous shear, wall slip, and shear banding of entangled polymeric liquids in simple-shear rheometry: A roadmap of nonlinear rheology," Macromolecules **44**, 183–190 (2011).
[17] Ravindranath, S., S.-Q. Wang, M. Ofechnowicz, and R. P. Quirk, "Banding in simple steady shear of entangled polymer solutions," Macromolecules **41**, 2663–2670 (2008).
[18] Yerushalmi, J., S. Katz, and R. Shinnar, "The stability of steady shear flows of some viscoelastic fluids," Chem. Eng. Sci. **25**, 1891–1902 (1970).

[19] Lee, C.-S., B. C. Tripp, and J. J. Magda, "Does N1 or N2 control the onset of edge fracture?," Rheol. Acta **31**, 306–308 (1992).

[20] Inn, Y. W., K. F. Wissbrun, and M. M. Denn, "Effect of edge fracture on constant torque rheometry of entangled polymer solutions," Macromolecules **38**, 9385–9388 (2005).

[21] Sui, C., and G. B. McKenna, "Instability of entangled polymers in cone and plate rheometry," Rheol. Acta **46**, 877–888 (2007).

[22] Schweizer, T., and M. Stöckli, "Departure from linear velocity profile at the surface of polystyrene melts during shear in cone-plate geometry," J. Rheol. **52**, 713–727 (2008).

[23] Mattes, K. M., R. Vogt, and C. Friedrich, "Analysis of the edge fracture process in oscillation for polystyrene melts," Rheol. Acta **47**, 929–942 (2008).

[24] Jensen, E. A., and J. C. Christiansen, "Measurements of first and second normal stress differences in a polymer melt," J. Non-Newtonian Fluid Mech. **148**, 41–46 (2008).

[25] Dai, S.-C., E. Bertevas, F. Qi, and R. I. Tanner, "Viscometric functions for noncolloidal sphere suspensions with Newtonian matrices," J. Rheol. **57**, 493–510 (2013).

[26] Tanner, R. I., and M. Keentok, "Shear fracture in cone-plate rheometry," J. Rheol. **27**, 47–57 (1983).

[27] Keentok, M., and S.-C. Xue, "Edge fracture in cone-plate and parallel plate flows," Rheol. Acta **38**, 321–348 (1999).

[28] Hemingway, E. J., H. Kusumaatmaja, and S. M. Fielding, "Edge fracture in complex fluids," Phys. Rev. Lett. **119**, 028006 (2017).

[29] Hemingway, E. J., and S. M. Fielding, "Edge fracture instability in sheared complex fluids: Onset criterion and possible mitigation strategy," J. Rheol. **63**, 735–750 (2019).

[30] Britton, M. M., and P. T. Callaghan, "Shear banding instability in wormlike micellar solutions," Eur. Phys. J. B **7**, 237–249 (1999).

[31] Berret, J. F., G. Porte, and J. P. Decruppe, "Inhomogeneous shear rows of wormlike micelles: A master dynamic phase diagram," Phys. Rev. E **55**, 1668–1676 (1997).

[32] Tapadia, P., and S.-Q. Wang, "Direct visualization of continuous simple shear in non-newtonian polymeric fluids," Phys. Rev. Lett. **96**, 016001 (2006).

[33] Hu, Y. T., L. Wilen, A. Philips, and A. Lips, "Is the constitutive relation for entangled polymers monotonic?," J. Rheol. **51**, 275–295 (2007).

[34] Hu, Y. T., "Steady-state shear banding in entangled polymers?," J. Rheol. **54**, 1307–1323 (2010).

[35] Sui, C., and G. B. McKenna, "Instability of entangled polymers in cone and plate rheometry," Rheol. Acta **46**, 877–888 (2007).

[36] Wang, S.-Q., G. Liu, S. Cheng, P. E. Boukany, Y. Wang, and X. Li, "Letter to the editor: Sufficiently entangled polymers do show shear strain localization at high enough Weissenberg numbers," J. Rheol. **58**, 1059–1069 (2014).

[37] Li, Y., M. Hu, G. B. McKenna, C. J. Dimitriou, G. H. McKinley, R. M. Mick, D. C. Venerus, and L. A. Archer, "Response to: Sufficiently entangled polymers do show shear strain localization at high enough Weissenberg numbers," J. Rheol. **58**, 1071–1082 (2014).

[38] Johnson, Jr., M. W., and D. Segalman, "A model for viscoelastic fluid behavior which allows non-affine deformation," J. Non-Newtonian Fluid Mech. **2**, 255–270 (1977).

[39] Giesekus, H., "A simple constitutive equation for polymer fluids based on the concept of deformation-dependent tensorial mobility," J. Non-Newtonian Fluid Mech. **11**, 69–109 (1982).

[40] David Lu, C.-Y., P. D. Olmsted, and R. C. Ball, "Effects of nonlocal stress on the determination of shear banding flow," Phys. Rev. Lett. **84**, 642–645 (2000).

[41] Bray, A. J., "Theory of phase-ordering kinetics," Adv. Phys. **43**, 357–459 (1994).

[42] Kusumaatmaja, H., E. J. Hemingway, and S. M. Fielding, "Moving contact line dynamics: From diffuse to sharp interfaces," J. Fluid Mech. **788**, 209–227 (2016).

[43] Yue, P., C. Zhou, and J. J. Feng, "Sharp-interface limit of the Cahn–Hilliard model for moving contact lines," J. Fluid Mech. **645**, 279–294 (2010).

[44] Dong, S., "On imposing dynamic contact-angle boundary conditions for wall-bounded liquid–gas flows," Comput. Methods Appl. Mech. Eng. **247–248**, 179–200 (2012).

[45] Dimitriou, C. J., L. Casanellas, T. J. Ober, and G. H. McKinley, "Rheo-PIV of a shear-banding wormlike micellar solution under large amplitude oscillatory shear," Rheol. Acta **51**, 395–411 (2012).

[46] Schweizer, T., "Shear banding during nonlinear creep with a solution of monodisperse polystyrene," Rheol. Acta **46**, 629–637 (2007).

[47] Ricci, E., R. Sangiorgi, and A. Passerone, "On the measurement of the surface tension of DNA solutions," J. Colloid Interface Sci. **102**, 295–297 (1984).

[48] Boukany, P. E., and S.-Q. Wang, "Exploring the transition from wall slip to bulk shearing banding in well-entangled DNA solutions," Soft Matter **5**, 780–789 (2009).

[49] Adams, J. M., and P. D. Olmsted, "Nonmonotonic models are not necessary to obtain shear banding phenomena in entangled polymer solutions," Phys. Rev. Lett. **102**, 067801 (2009).